Tb³⁺/Pr³⁺ co-doped ZnMoO₄ phosphor with tunable photoluminescence and energy transfer processes

L.X. Lovisa[a,*], Y.L.R.L. Fernandes[a], L.M.P. Garcia[a], B.S. Barros[b], E. Longo[c], C.A. Paskocimas[a], M.R.D. Bomio[a], F.V. Motta[a]

[a] *LSQM, Laboratory of Chemical Synthesis of Materials, Department of Materials Engineering, Federal University of Rio Grande do Norte, P.O. Box 1524, 59078-900, Natal, RN, Brazil*
[b] *Federal University of Pernambuco, Mechanical Engineering Department, Av. Prof. Moraes Rego-1235, University City, Recife, PE, Brazil*
[c] *CDMF-LIEC, UFSCar, P.O. Box 676, 13565-905, São Carlos, SP, Brazil*

ABSTRACT

ZnMoO₄:Tb³⁺, Pr³⁺ particles in different Tb:Pr ratios (2:0, 1.5:0.5, 1:1, 0.5:1.5 and 0:2) were synthesized by the sonochemical method. These materials were characterized structurally, morphologically and optically by X-ray diffraction (XRD), Field Emission Scanning Electron Microscopy (FESEM), Ultraviolet–visible absorption spectroscopy and Photoluminescence (PL). From studying the photoluminescent properties, the PL spectra presented $^5D_4 \rightarrow {}^7F_j$ (j = 6, 5, 4 and 3) transitions bands of Tb³⁺, along with the transitions $^3P_0 \rightarrow {}^3H_5$, $^1D_2 \rightarrow {}^3H_4$, $^3P_0 \rightarrow {}^3H_6$ and $^3P_0 \rightarrow {}^3F_3$ of Pr³⁺. Time resolved photoluminescence was investigated and an energy transfer (***n***) mechanism between the matrix and the Tb³⁺ and Pr³⁺ ions is simultaneously proposed for better understanding the process efficiency. Parallel to this perspective, the photocatalytic behavior of ZnMoO₄:Tb³⁺, Pr³⁺ was evaluated. The degradation of methylene blue dye was favored by the effect of increasing the Pr³⁺ concentration. This work deals with the development of inorganic phosphor materials capable of converting UV radiation into light-emitting diode, which can be suitably combined to produce white light.

1. Introduction

Molybdates were doped with **R**are **E**arth elements (**RE**) to form a family of materials which present different types of crystalline structures. The RE and clusters [MoOn] have not only become important in researching new materials due to fundamental scientific interests, but also for their possible application in various technological areas [1–6]. Above all, molybdates with different types of clusters [MoOₙ] show great luminescence when used as the host matrix for WLEDs because of their excellent optical, chemical and structural properties: broad emission spectrum (UV–Visible–NIR), high refraction, high color purity index, strong charge transfer between the bands of the 2p (O²⁻) and 4d (Mo⁶⁺) activated orbitals and the structural diversity of these materials [7–9].

Zinc molybdate (ZnMoO₄) is a semiconducting material which can be in two different types of structure, either (α) triclinic and (β) monoclinic depending upon the processing parameters. α-ZnMoO₄ possesses a triclinic structure with point group symmetry C1 and space group P1. All zinc atoms (Zn) are bound to six oxygen atoms (O), forming distorted octahedral clusters [ZnO₆]. The molybdenum atoms

(Mo) are coordinated to four O atoms, resulting in tetrahedral clusters [MoO₄] [10,11]. The β-ZnMoO₄ crystal has a wolframite-type monoclinic structure belonging to a P2/c space group and point group symmetry C_{2h}^4. In the β-ZnMoO₄ monoclinic structure, the Zn and Mo atoms are bound to six O atoms which promote the origin of distorted octahedral clusters [ZnO₆]/[MoO₆] [12].

ZnMoO₄ has recently been extensively studied due to its importance in technological application in the field of photoluminescence, photocatalytic, cryogenic/bolometric scintillation detectors, anticorrosive pigments and electrodes in lithium batteries [3,13–16]. Specifically, photoluminescent and photocatalytic properties are potentiated from adding RE into the ZnMoO₄ matrix [10]. RE especially acts by increasing or decreasing the recombination rate between the electron - hole (ē + h) in the band gap thereby favoring the photoluminescent and photocatalysis, respectively [17].

In this work, the ZnMoO₄:Tb³⁺, Pr³⁺ phosphor series was prepared using the sonochemical method. The effects of the dopant concentration were evaluated on the morphological, photoluminescent and photocatalytic properties. the adjustment of the color emitted in the blue and white regions by the control of Tb³⁺% and Pr³⁺% was also

---

investigated. Finally, an energy transfer mechanism between the [MoO$_4$], Tb^{3+} and Pr^{3+} matrix is proposed to explain the behavior presented in the emission spectra of PL. Through the proposed characterizations, this study shows that ZnMoO$_4$:Tb^{3+}, Pr^{3+} presents relevant results for applications in the photoluminescence and pigment degradation fields, highlighting the influence of dopants in the studied processes.

2. Experimental

2.1. Materials

Molybdic acid (H$_2$MoO$_4$) (Alfa Aesar), zinc nitrate (Zn(NO$_3$)$_2$.6H$_2$O) (Synth), terbium oxide (Tb$_4$O$_7$) (Aldrich), Praseodymium(III) nitrate (Pr (NO$_3$)$_3$.xH$_2$O) (Alfa Aesar), nitric acid (Synth), ammonium hydroxide (NH$_4$OH) (Synth) and distilled water were used as received to prepare the ZnMoO$_4$ and ZnMoO$_4$:Tb, Pr particles.

2.2. Sonochemical synthesis of the ZnMoO$_4$ and ZnMoO$_4$:Tb^{3+}, Pr^{3+} particles

The Tb$_4$O$_7$ oxide was initially dissolved separately in 10 ml of nitric acid to obtain their respective nitrate. This element is insoluble in the reaction medium once in the oxide form. Two precursor solutions were prepared for the synthesis of the ZnMoO$_4$ and ZnMoO$_4$:Tb^{3+}, Pr^{3+} particles: one of molybdenum (solution A) and the other of zinc (solution B), with a molar ratio of 1:1. The starting reagent was dissolved in 40 ml of distilled water for both solutions. Solution B was added to the solution by dripping it and under constant magnetic stirring. Then the dopants were added one at a time. Finally, NH$_4$OH was added to the solution to stabilize its pH at 8, observing the formation of the precipitate. The final solution was exposed to intense ultrasonic radiation [10,18,19] with a 65% amplitude in the continuous mode for 30 min. The solution was centrifuged three times in distilled water and then kept in the oven at a temperature of 80 °C for 24 h for drying. The particles were calcined at 450 °C for 4 h at a heating rate of 10 °C/min.

In the synthesis of ZnMoO$_4$ and ZnMoO$_4$:Tb^{3+}, Pr^{3+}, the amounts of the regents used were stoichiometrically weighed according to the values presented in Table 1. Energy dispersive X-ray spectroscopy (EDS) was performed to verify the chemical composition of the samples. The presence of doping ions (Tb^{3+}, Pr^{3+}) in the ZnMoO$_4$ matrix is observed. It is possible to verify the homogeneous distribution of the Tb^{3+}, Pr^{3+} ions in all ZnMoO$_4$ particles by mapping the distribution of the elements. This material homogeneity is of great importance for the efficiency of the photoluminescent behavior according to the results presented in this work. The EDS spectrum figure and atom distribution mapping were included (see Fig. S1, Supplementary Information).

2.3. Characterizations

The ZnMoO$_4$ and ZnMoO$_4$:Tb^{3+}, Pr^{3+} particles were structurally characterized by XRD using a Shimadzu XRD 7000 instrument with Cu-Ka radiation (λ = 1.5406 Å) in the 2θ range from 10 to 50° at a scanning rate of 0.02 s^{-1}. The morphologies were investigated using a field-emission gun scanning electron microscopy (FEG-SEM; Carl Zeiss,

Table 1
ZnMoO$_4$: Tb^{3+}, Pr^{3+} compositions investigated.

Zinc Molybdate (ZnMoO$_4$) (%)	Terbium (Tb) (%)	Praseodymium (Pr) (%)
100	0	0
98	2	0
98	0	2
98	1.5	0.5
98	1	1
98	0.5	1.5

Supra 35- VP Model, Germany) operated at 6 kV. The UV–vis diffuse reflectance spectrum was measured at room temperature using a UV–vis spectrometer. The photoluminescence (PL) spectra were acquired with an Ash Monospec 27 monochromator (Thermal Jarrel, U.S.A.) and a R4446 photomultiplier (Hamamatsu Photonics, U.S.A.). The 350 nm beam of a krypton ion laser (Coherent Innova 90 K) was used as the excitation source, while its maximum output power was kept at 200 mW. All measurements were performed at room temperature. The time decay measurements were performed on a Fluorolog3 Horiba Jobin Yvon spectrofluorometer equipped with Hamamatsu R928P photomultiplier, SPEX 1934 D phosphorimeter, and a pulsed 150 W XeeHg lamp.

The photocatalytic properties of the powders combined as a catalyst agent were estimated by the degradation of the methylene blue dye (MB) with a molecular formula [C$_{16}$H$_{18}$ClN$_3$S] (99.5% purity, Mallinckrodt), illuminated by UV lamps, in aqueous solution. First, 50 ml of the MB solution (1 × 10^{-5} mol L^{-1} concentration) was mixed with 0.05 g of the material to be tested in a quartz beaker. This mixture was kept under stirring at a controlled temperature (25 °C) and lit by six UVC lamps (15 W TUV Philips, with maximum intensity of 254 nm = 4.9 eV). The sample was kept under stirring for 30 min with the lights off to disregard possible adsorption events. An aliquot of the samples were taken at each 30-min time interval and centrifuged at 9000 rpm for 5 min to remove the suspended particles. Finally, the variations of the maximum absorption band of each aliquot were measured by UV–Vis absorbance with spectral measurements using a Shimadzu UV-2600 spectrophotometer with a wavelength in the range of 400–800 nm.

Reproducibility of the technological process in the syntheses of ZnMoO$_4$:Tb^{3+}, Pr^{3+} particles was achieved during the study. Our group has been working with several types of molybdates in different study periods [10,11,18,19] and has respected the reproducibility factor in the experiments and the characterizations of the samples. The UV–vis and PL spectra are customized for the samples to ensure measurement performance.

3. Results and discussion

3.1. X-ray diffraction

It was possible to verify the degree of order-disorder structural at the long-range distances from the XRD technique and the structural periodicity of the ZnMoO$_4$:Tb^{3+}, Pr^{3+} particles. Fig. 1 (a) shows the influence of dopant percentage on the ZnMoO$_4$ lattice synthesized by sonochemistry and calcined at 450 °C for 4 h. All ZnMoO$_4$:Tb^{3+}, Pr^{3+} diffraction peaks can be indexed considering the triclinic structure with space group P-1 and symmetry C1 of the α-ZnMoO$_4$ phase with JCPDS card no. 35–0765 and having six molecules per unit cell (Z = 6).

It is observed in Fig. 1 (b) that the diffraction peak (120) located at 24.43° is slightly shifted to the low angle region for the doped samples, consequently resulting in greater interplanar distances and causing a slight increase in the volume of the unit cell. This displacement is caused by the ZnMoO$_4$ lattice distortion as a function of the substitution of Zn^{2+} → Tb^{3+}/Pr^{3+} cations [20]. The changes in the values of the lattice parameters and the unit cell volume are related to the difference in the ionic radii sizes of the cations. The Zn^{2+} ion has an ionic radius equal to 0.900 Å and the Tb^{3+} and Pr^{3+} ions present ionic radii equal to 0.93 Å and 1 Å, respectively. As calculated values of lattice parameters and crystallite size depend on diffractions angles, alterations of both in agreement with the variation of the angle are expected. The mean crystallite size was estimated by the Scherrer equation (1) using the full width at half maximum (FWHM) of the diffraction peak (120).

$$D = \frac{0.89\lambda}{\beta Cos\theta} \tag{1}$$

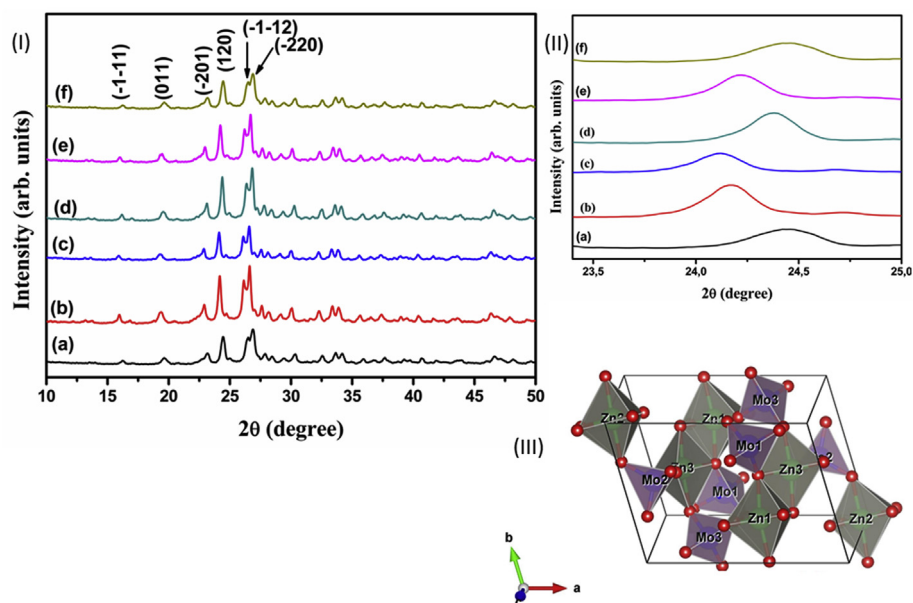where D is the average crystalline size, λ is the wavelength of X-rays

Fig. 1. X-ray diffraction of the $ZnMoO_4$ and $ZnMoO_4:Tb^{3+}$, Pr^{3+} particles.

Table 2
Lattice parameters, cell unit volume and crystallite sizes of the $ZnMoO_4$ and $ZnMoO_4:Tb^{3+}$, Pr^{3+} particles and values of JCPDS card no. 35–0765.

Samples	a (nm)	b (nm)	c (nm)	α (°)	β (°)	γ (°)	V(Å)³	D (Å)
$ZnMoO_4$	9.7036	6.9681	8.3773	101.76	96.73	106.84	566.4366	435.49
$ZnMoO_4$: 2% Tb	9.7035	6.9674	8.3746	101.71	96.74	106.85	566.1913	632.68
$ZnMoO_4$: 2% Pr	9.6903	6.9554	8.3872	101.72	96.71	106.82	565.2965	683.37
$ZnMoO_4$: 0.5% Pr 1.5% Tb	9.6953	6.9638	8.3717	101.77	96.76	106.83	565.2247	545.77
$ZnMoO_4$: 1% Pr 1% Tb	9.7054	6.9706	8.3795	101.76	96.74	106.83	566.8937	547.04
$ZnMoO_4$: 1.5% Pr 0.5% Tb	9.7090	6.9768	8.3818	101.7308	96.73	106.81	567.7642	389.13
Card JCPDS no. 35-0765	**9.6916**	**6.9643**	**8.3678**	**101.726**	**96.734**	**106.872**	**564.7864**	**-**

(0.15405 nm), β is the full height at half maximum of the diffraction peak (FWHM) and θ is the diffraction angle. The values of the lattice parameters, unit cell volume, and crystallite size of $ZnMoO_4$ were in accordance with those of the JCPDS database (No. 35–0765) as recorded in Table 2.

Small differences in the lattice parameters of the samples are observed, and these slight discrepancies may also be related to residual stresses induced by the conditions of sonochemical preparation.

Fig. 1 (c) shows the unit cell representation of $ZnMoO_4$ from the positions of the atoms in the lattice by the VESTA program. Polyhedral coordination is verified, in which the zinc ion has an octahedral coordination by oxygen atoms $[ZnO_6]$ and the molybdenum ion are coordinated by four oxygen atoms $[MoO_4]$.

3.2. Field Emission Scanning Electron Microscopy (FEG-SEM)

Fig. 2 shows the FEG-SEM images of the samples obtained by the sonochemical method. The pH value for all syntheses performed was adjusted to 8.0, and the proportion of the amount of the precursors used was also kept constant $[Zn^{2+}]$: $[MoO_4]^{2-}$ = 1:1. Fig. 2(a) shows the morphology of $ZnMoO_4$ particles with the presence of microspherical particles with a diameter of about 1.2 μm. In Fig. 2 (b, c) with high magnification images, it is observed that these microspheres consist of numerous nanosized particles of irregular shapes. Fig. 2(d–f) refers to the image of the $ZnMoO_4:2\%$ Tb^{3+} sample, in which it was observed that there were no large variations in the morphology of the particles compared to the non-doped $ZnMoO_4$. Fig. 2(g–i) corresponds to the image of the $ZnMoO_4:2\%$ Pr^{3+} sample with the appearance of nanorod-shaped particles, indicating oriented growth. These particles appear even more discrete along with nanoparticles of irregular shapes. This

sensitive tendency of change in morphology indicates a disposition to directed growth possibly caused by the presence of the Pr^{3+} dopant in the $ZnMoO_4$ structure.

The particle growth scheme is described in Fig. 3. The growth proposal for the $ZnMoO_4$ crystals is based on the following steps: dissolution and recrystallization → growth → self-assembly. The precursors (H_2MoO_4, $Zn(NO_3)_2.6H_2O$) were initially dissolved in aqueous medium separately. By adding the Zn solution to the (MoO_4) solution and adjusting the pH to 8, the Zn^{2+} ions can react with (MoO_4)$^{2-}$, thereby forming numerous $ZnMoO_4$ nuclei. After the nuclei reach a critical size acquiring thermodynamic stability, they begin to aggregate, initiating the growth stage of the particles. In looking at the FEG-SEM images in Fig. 2 it can be seen that the particles of the $ZnMoO_4$ and $ZnMoO_4:2\%$ Tb^{3+} group go through a growth known as coarsening [21]. The nanoparticles participate in the self-assembly process generating a microsphere structure with the objective of reducing the surface energy [22]. Particles with larger sizes (i.e., Ostwald ripening) are part of a common process in various nanomaterials. This mechanism is based on reactions of particle dissolution and recrystallization of ions as a function of crystal size, and consequently as a function of their solubility, as described by the Thompson-Freundlich equation [23]. Coalescing growth generally produces quasi-spherical morphologies, which are thermodynamically more stable because of the total surface energy minimization [24]. The $ZnMoO_4:2\%$ Pr^{3+} particles show anisotropic growth, indicating a preference for growth direction. Anisotropy is obtained by controlling the kinetics of the growth processes following nucleation. After this behavior, $ZnMoO_4:2\%$ Pr^{3+} particles exhibited nanorod morphology. Anisotropic nanostructures such as nanowires and nanobastones are of great interest, since the effects of quantum confinement on systems are also dependent on form. Thus,
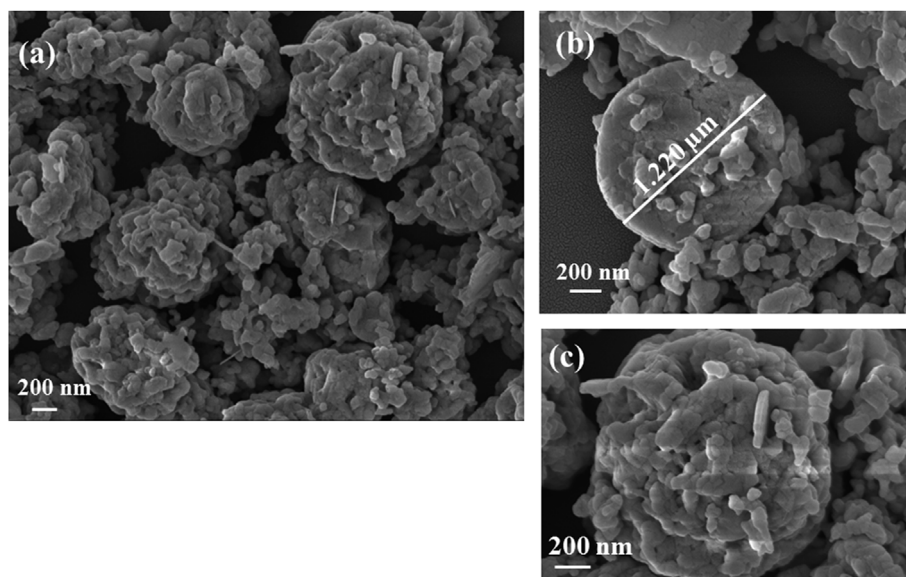
Fig. 2. FEG-SEM micrographs of $ZnMoO_4$ and $ZnMoO_4$:Tb^{3+}, Pr^{3+} particles prepared by the sonochemical method, $ZnMoO_4$ (a–c), $ZnMoO_4$:2% Tb^{3+} (d–f), $ZnMoO_4$:2%Pr^{3+} (g–i).

semiconductor nanobesters should offer improvements in the performance of solar cell devices, gas sensors and catalysts [25–27].

3.3. Uv–vis

From the absorption of Uv–vis, it is possible to analyze and observe the appearance of intermediate energy levels within the band gap promoted by the presence of defects and/or distortions in the lattice. These imperfections are implications of the synthesis conditions (temperature, pressure), synthesis method, impurities and dopant [28].

The absorption spectra of the $ZnMoO_4$ and $ZnMoO_4$:Tb^{3+}, Pr^{3+} samples was recorded within the region of 200–800 nm and is shown in Fig. 4. The spectra exhibited a wide absorption range between 200 and 375 nm. This behavior suggests that the emission process occurred by multi-energy process in clusters [MoO_4] [29]. The appearance of bands

centered at 446, 487, 595 and 616 nm are observed, which are attributed to the emergence of the transitions: $^5D_3 \rightarrow {}^7F_3$ (Tb^{3+}), $^5D_4 \rightarrow {}^7F_4$ (Tb^{3+}), $^3P_0 \rightarrow {}^3H_5$ (Pr^{3+}), $^1D_2 \rightarrow {}^3H_4$ (Pr^{3+}). It was verified that the introduction of Tb^{3+} and Pr^{3+} ions into the $ZnMoO_4$ matrix occurred successfully. The displacements observed in the absorption spectra of the co-doped samples were promoted by the structural disorder and short range distortions by the substitution $Zn^{2+} \rightarrow RE^{3+}$, as mentioned in the XRD results.

The reflectance data were transformed through the Kubelka-Munk function (2) to determine the gap energy [30]. Thus, the F (R) function combined with the Tauc equation (3) was used to estimate the spacing between the conduction band and the valence of the synthesized material as follows:
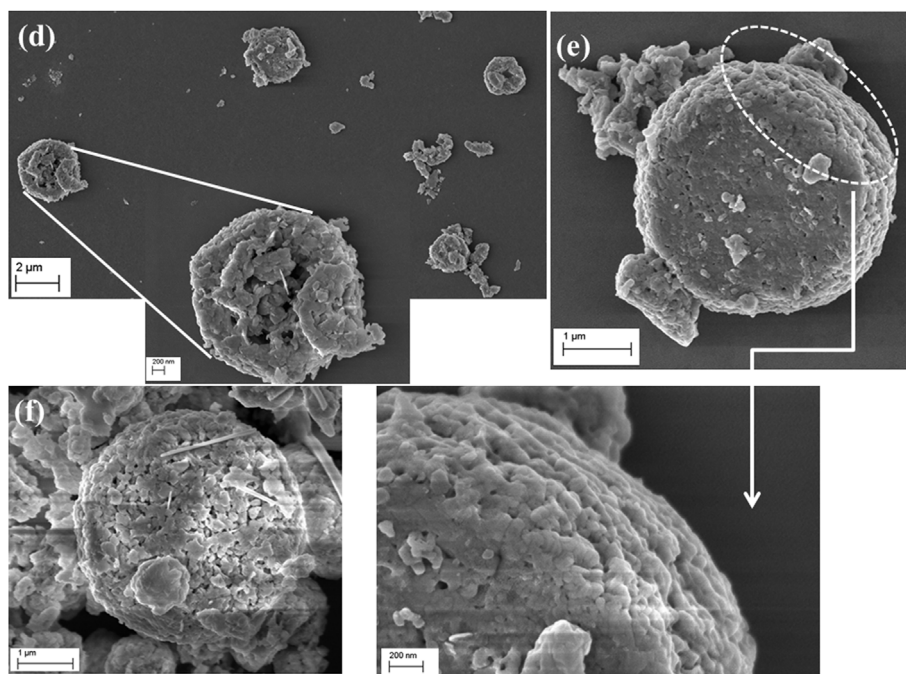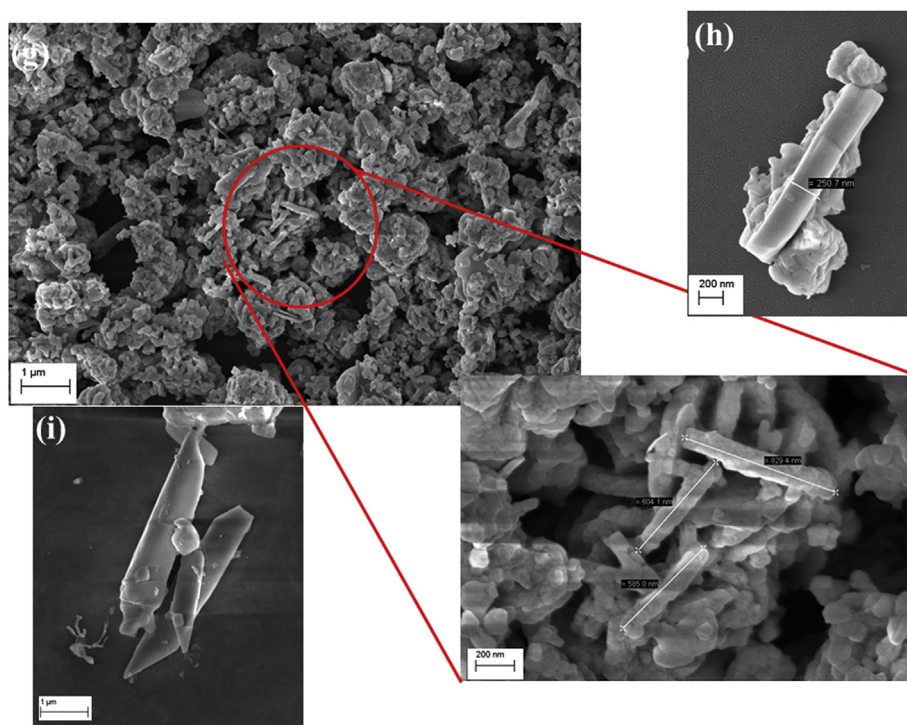

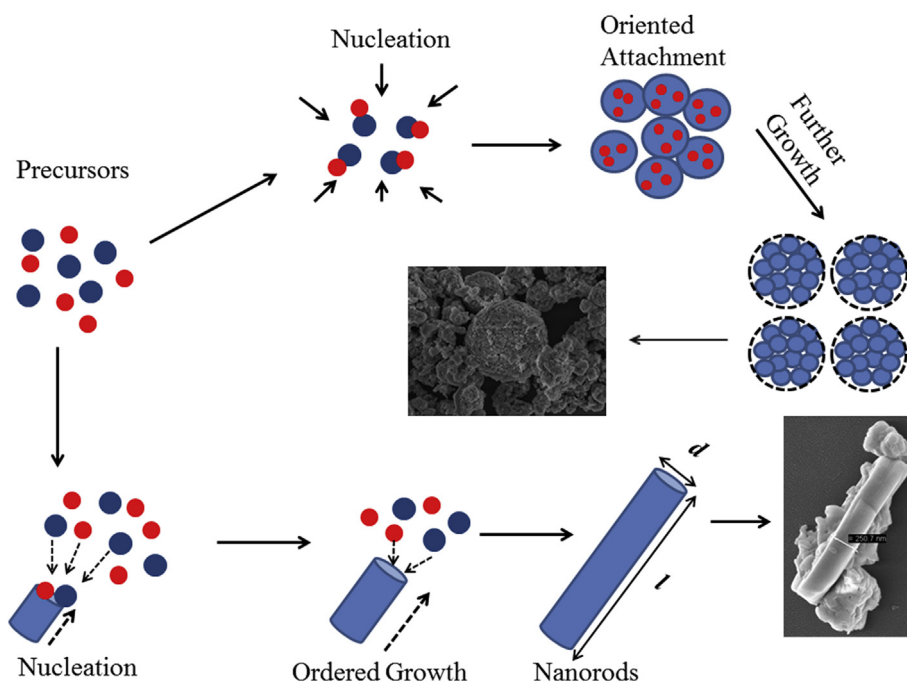**Fig. 2.** (*continued*)

Fig. 2. (*continued*)

Fig. 3. Schematic illustration for the possible formation of microspherical mechanisms and nanorods of ZnMoO$_4$.

$$F(R) = \frac{(1-R)^2}{2R} = \frac{\alpha}{s} \qquad (2)$$

where α is the optical absorption coefficient and s is the dispersion coefficient. The following equation is used to calculate the band gap energy:

$$(\alpha h\nu) = (h\nu - Eg)^n \qquad (3)$$

Where $h\nu$ is the energy of the incident photon and exponent n is the constant which represents different types of electronic transitions ($n = 0.5$ for direct allowed, $n = 1.5$ direct forbidden, $n = 2$ indirect

allowed and $n = 3$ indirect forbidden). According to Lacomba-Perales [31], Validzic [32] and Fuertes-Ruiz [33], zinc molybdate and zinc tungstate are governed by a direct type optical absorption. Hence we calculated the gap energy (Eg) of ZnMoO$_4$ using $n = 0.5$ in the present study.

The direct type transition is verified when the electron transition occurs between the bottom of the conduction band and the top of the valence band at the same point in the Brillouin zone [34]. Fig. 5 shows the graphs plotted between ($\alpha h\nu$) on the ordinate axis, and vs $h\nu$ on the abscissa axis of the samples. The extrapolation of the straight line to
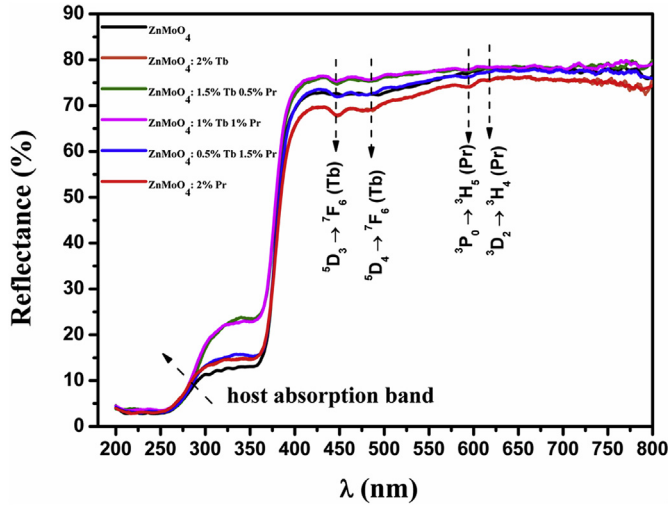
Fig. 4. Absorption spectra of the ZnMoO$_4$ and ZnMoO$_4$: Tb^{3+}, Pr^{3+} samples.

($\alpha h\nu$) = 0 gives the gap energy value. The estimated values for Eg of the samples in this work are between 4.15 and 4.26 eV as observed by linear region extrapolation. The obtained values are very consistent with those found in other studies. Spassky et al. [35] obtained the theoretical gap energy value of 4.30 eV for a single ZnMoO$_4$ crystal by the Czochralski method. Zhang et al. [36] obtained the energy value of gap of 3.64 eV for α-ZnMoO$_4$ prepared by the electrochemical method. Some factors may interfere with the value of Eg, such as: processing techniques, structural characteristics (degree of crystallinity, mean particle size, lattice parameter values).

A band around 3.2 eV (~390 nm) is observed in Fig. 5; this characteristic is associated with the presence of defects present in the ZnMoO$_4$ lattice. Zhai et al. [37] verified two absorption bands in a study on the optical characterization of ZnMoO$_4$:Eu^{3+}; the first in the 250–310 nm range was related to the electronic transitions between the valence band and the conduction band; while the second band was associated with the defects present in ZnMoO$_4$. Doping ZnMoO$_4$ with RE^{3+} ions significantly increased the population density of defects in the matrix. Assuming that the RE cation has +3 charge, the Kroger-Vink notation for the RE^{3+} defect reactions in ZnMoO$_4$ can be described by the following equation (4)

$$RE^{3+} + Zn_{Zn}^{x} \rightarrow RE_{Zn}^{\circ} + Zn_{i}^{\circ\circ} \tag{4}$$

Equation (4) indicates that a RE^{3+} ion replaces a Zn^{2+} site in ZnMoO$_4$, producing a positively charged defect RE_{Zn}° and another interstitial defect $Zn_{i}^{\circ\circ}$. Therefore, doping may significantly increase the population density of defects in the host matrix. According to Longo [38], the defects, which can be classified as shallow, are located just above the conduction band and their appearance occurs in the blue-green region. This type of defect is promoted by structural distortions in the [MoO$_4$] clusters. A second type of defect, which lies below the valence band and occurs in the orange-red region, is known as a deep type. The vacancies of oxygen and cations are classified as deep type defects. In the case of this work, the band related to the defects is located at approximately 390 nm, qualifying them as shallow defects.

3.4. Study of photoluminescence

Fig. 6 shows the emission spectra of the ZnMoO$_4$ and ZnMoO$_4$:Tb^{3+}, Pr^{3+} particles which were excited at λ = 350 nm at room temperature. In the case of the ZnMoO$_4$ sample, a very characteristic broadband profile of the zinc molybdate [39] is observed due to the electronic transitions occurring between the O (2p) → Mo (4d) orbitals.

The recombination of $\bar{e} + h$ pairs in clusters [MoO$_4$] is responsible for the emission bands of ZnMoO$_4$ [40]. During the excitation process, some electrons located near the valence band (VB) in the 2p orbitals of the O absorb energy (hν) and are promoted to unoccupied levels near the conduction band (CB) in Mo 4d orbitals. After some time, the electrons participate in emission processes involving the recombination phenomenon in centers located in the band gap. The increase in the recombination rate favors the intensity of the photoluminescence [41]. Cavalcante et al. [42] attributed the differences in the emission intensities of ZnMoO$_4$ crystals to changes in the morphology, crystal size and surface defects. Campos et al. [43] and Marques et al. [44] support the processes of CaMoO$_4$ particle emission basically by the existence of [MoO$_3$] and [MoO$_4$] distorted groups in the crystalline structure. This degree of order and disorder in the structure favors the appearance of localized levels of energy in the band gap, which consequently influences the photoluminescent properties. According to the ZnMoO$_4$ spectrum in Fig. 6, the band is centered around 410 nm with a larger contribution in the blue region.

The distortions and disorders generated as a result of the synthesis conditions create several intrinsic defects in the material. The multi-
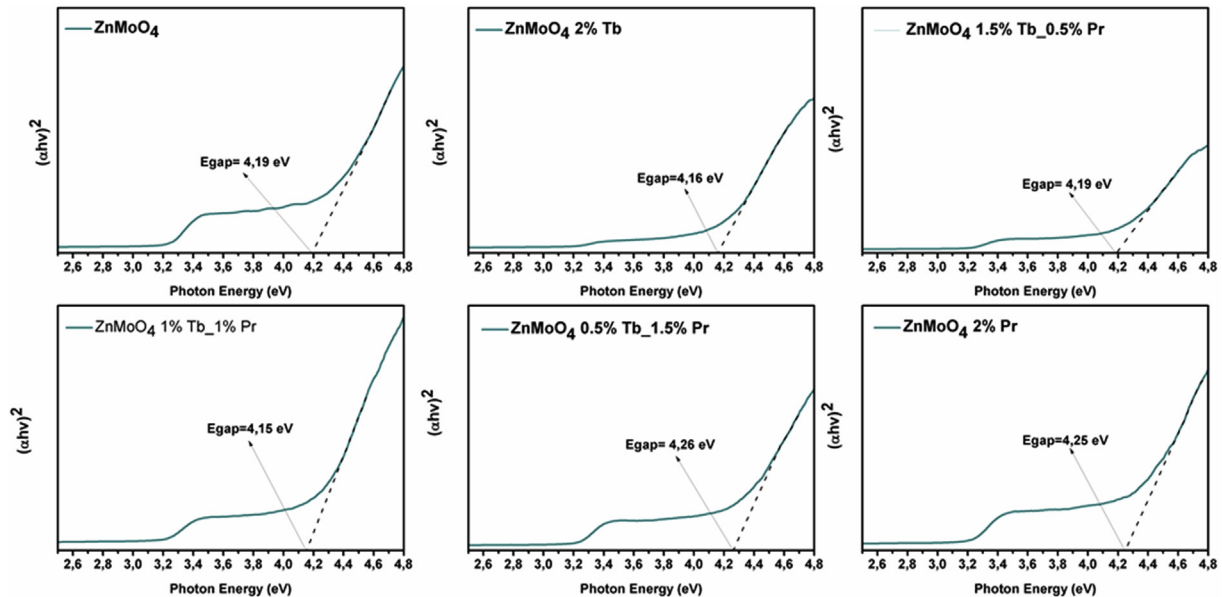

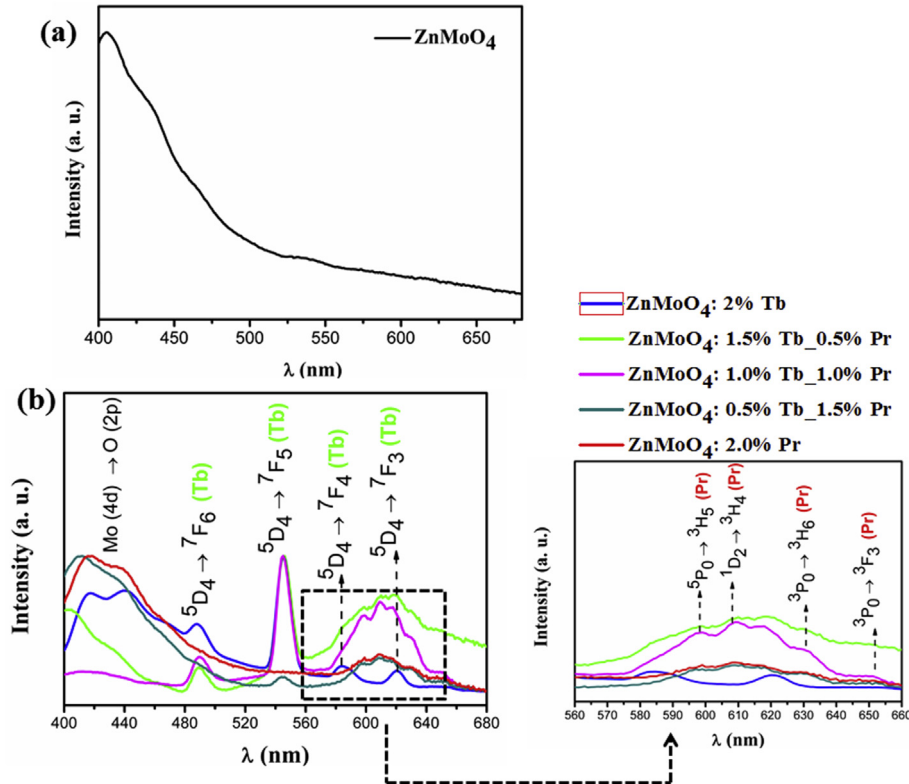**Fig. 5.** Gap energy of ZnMoO$_4$ and ZnMoO$_4$:Tb^{3+}, Pr^{3+} samples.

Fig. 6. Emission spectra of ZnMoO$_4$ and of ZnMoO$_4$:Tb^{3+}, Pr^{3+}.

phonon or multilevel processes occur in the materials due to the presence of these defects, leading to a broader emission spectrum [45]. In some studies, it is reported that ZnMoO$_4$ is considered to be one of the ABO$_4$ (A = Ca, Zn, Cd, Pb and B = Mo, W) self-activating phosphors, where photoluminescent emission is motivated by transitions of charge transfer within the $[MoO4]^{2-}$ [46] complexes.

The spectra of the ZnMoO$_4$:Tb^{3+}, Pr^{3+} samples show a broad band between 400 and 480 nm associated with the matrix interference and the specific transitions of Tb^{3+} and Pr^{3+}. The transitions related to Tb^{3+} are $^5D_4 \rightarrow {}^7F_j$ (j = 6, 5, 4 and 3) located at 487, 545, 584 and 621 nm, respectively [47]. The transitions of Pr^{3+} are $^3P_0 \rightarrow {}^3H_5$, $^1D_2 \rightarrow {}^3H_4$, $^3P_0 \rightarrow {}^3H_6$ and $^3P_0 \rightarrow {}^3F_3$, respectively located at 598, 609, 630 and 650 nm [48], as highlighted in Fig. 6.

The chromaticity coordinates (CIE) were calculated according to the distribution of the photoluminescence emission spectra. In order to characterize the emitted color, the correlative color temperature (CCT) and the color reproducibility index (CRI) were also evaluated. The CIE diagram is shown in Fig. 7. Moreover, the parameters that characterize the colors emitted by the samples are recorded in Table 3.

The ZnMoO$_4$:1.5% Tb 0.5% Pr, ZnMoO$_4$:1% Tb 1% Pr and ZnMoO$_4$:0.5% Tb 1.5% Pr samples show emissions in white due to adjusted cooperation in the regions: blue (influenced by matrix), green (Tb^{3+} emissions) and red (emissions of Pr^{3+}), as shown in the emission spectra of PL. This behavior demonstrates that the control in the dopant composition is important for modulating the characteristics of the colors emitted by the matches. Based on these results, they are strong candidates for applications in WLEDs.

A decrease in the ZnMoO$_4$:1% Tb^{3+} 1% Pr^{3+} band intensity is observed as an indication of the energy transfer efficiency between matrix → Tb and Pr (ET1 and ET2) and between Tb^{3+} → Pr^{3+} (ET3). The matrix assumes the receptor function (**R**) and transfers part of the absorbed energy to the activating ions (**A**). The ETs are affected by the decrease of Tb^{3+} type activating ions, which have an energy level closer to the matrix, leading to a transfer of energy. Since the energy levels of the Pr^{3+} are very far from the matrix, this favors the

absorption and emission by ZnMoO$_4$ itself. Fig. 8 illustrates the ZnMoO$_4$:Tb^{3+}, Pr^{3+} levels diagram with possible electronic transitions and energy transfer in order to explain the probable phenomena involved in them.

The luminescence decay curves of ZnMoO$_4$ and ZnMoO$_4$:Tb^{3+}, Pr^{3+} phosphors (λ_{ex} = 350 nm and λ_{em} = 545 nm) were measured at room temperature to further identify the ET between Tb^{3+} and Pr^{3+}, as shown in Fig. 9. The decay curves of ZnMoO$_4$:Tb^{3+}, Pr^{3+} phosphors can be well fitted by a double-exponential function given in equation (5) [49].

$$I(t) = I_0 + A_1 e^{\left(-t/\tau_1\right)} + A_2 e^{\left(-t/\tau_2\right)} \qquad (5)$$

where I(t) corresponds to the luminescence intensity at time t and I_0 represents the initial intensity; A_1 and A_2 are the fitting parameters, both τ_1 and τ_2 are components of the decay time as a long lifetime and a short lifetime, respectively.

The double exponential behavior indicates the heterogeneous distribution of rare earth ions in the ZnMoO$_4$:Tb^{3+}, Pr^{3+} phosphors. The average lifetime can be evaluated by the next equation (6):

$$\tau_{av} = \frac{(A_1 \tau_1^2 + A_2 \tau_2^2)}{(A_1 \tau_1 + A_2 \tau_2)} \qquad (6)$$

From Equation (6) and Fig. 9, the effective lifetime values for ZnMoO$_4$, ZnMoO$_4$:2% Tb^{3+}, ZnMoO$_4$:1.5% Tb^{3+} 0.5% Pr^{3+}, ZnMoO$_4$:1% Tb^{3+} 1% Pr^{3+} and ZnMoO$_4$:0.5% Tb^{3+} 1.5% Pr^{3+} were calculated as 0.6483 ms, 1.0344 ms, 0.841 ms, 0.807 ms and 0.4422 ms, respectively.

It is observed that the sample doped with only Tb^{3+} presented a longer decay time of τ_{av} = 1.0344 ms. However, there is a decrease of τ_{av} after gradually adding the percentage of Pr^{3+}, reaching a minimum value of τ_{av} = 0.4422 ms for the ZnMoO$_4$:0.5% Tb^{3+} 1.5% Pr^{3+} sample. This behavior can be understood by a greater interaction between the Tb^{3+} and Pr^{3+} ions. The energy transfer efficiency (**n**) can be calculated using equation (7):
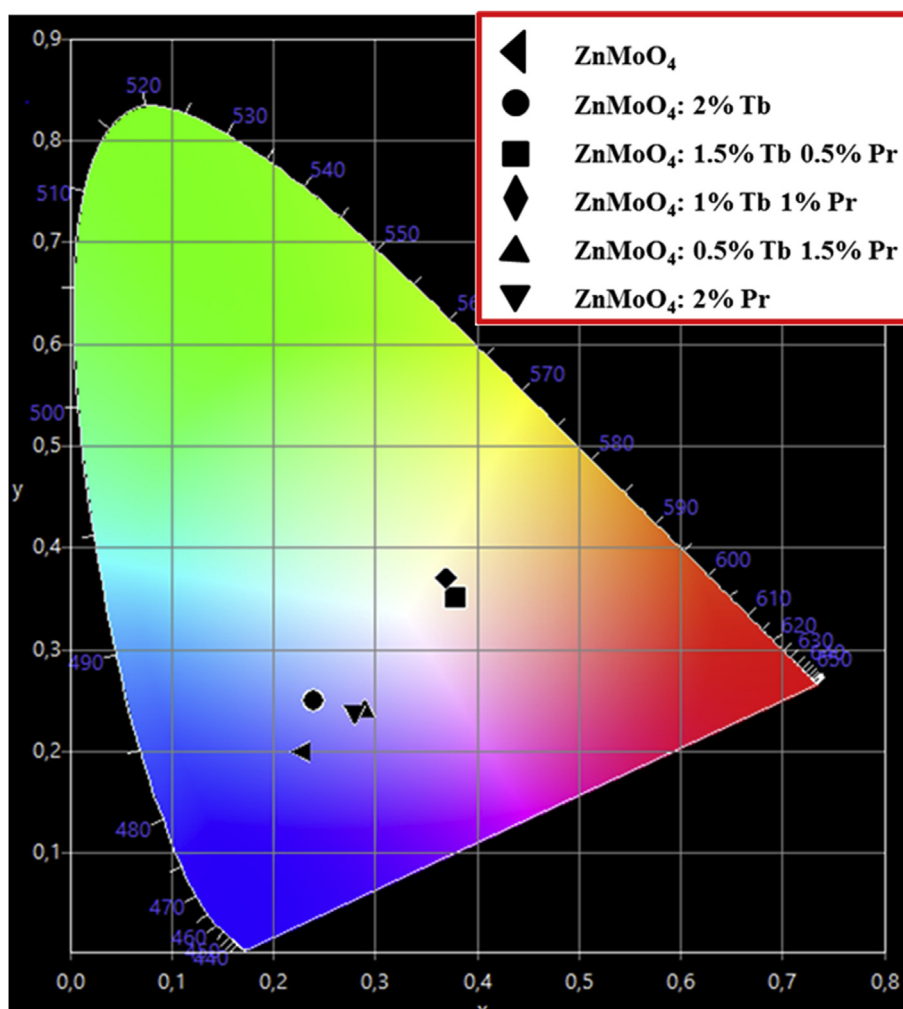
Fig. 7. Chromaticity diagram.

Table 3
CIE coordinates, CCT and CRI of the $ZnMoO_4$ and $ZnMoO_4:Tb^{3+}$, Pr^{3+} particles.

Samples	X	y	Color	CCT (K)	CRI (%)
$ZnMoO_4$	0.23	0.20	Blue	–	70
$ZnMoO_4$: 2% Tb	0.24	0.25	Blue	–	72
$ZnMoO_4$: 1.5% Tb 0.5% Pr	0.38	0.35	White	3723	94
$ZnMoO_4$: 1% Tb 1% Pr	0.37	0.36	White	4062	95
$ZnMoO_4$: 0.5% Tb 1.5% Pr	0.29	0.24	Blue	13328	71
$ZnMoO_4$: 2% Pr	0.28	0.24	Blue	16698	76

$$n = 1 - \frac{\tau_d}{\tau_0} \qquad (7)$$

In which τ_d and τ_0 are the decay times of the doped and non-doped samples, respectively. The most significant value of n was for the $ZnMoO_4$:0.5% Tb^{3+} 1.5% Pr^{3+} sample with 32% energy transfer efficiency.

The luminescence result depends on the recombination rate of the excessive charges (electron + hole) produced by the initial excitation. The lifetime can generally decrease with the increase of these trap centers. The decay rate is controlled by the excessive lifetime that these electronic pairs have and by the concentration level of the excessive loads. The afterglow is essentially a phosphorescent process. This process results from electron trapping or holes from lattice defects, preventing the immediate recombination of the electron-hole pair and decreasing the amount of energy transferred to the luminescence centers. The amount of energy stored depends on the nature and density of the traps in the structure. The phosphorescent materials have an ability to absorb and store energy and then emit the photons in long decay times.

The molybdates are characterized by the similar type of emission centers, which are the self-activated complexes $[MoO_4]^{2-}$ with characteristic decay time of 10^{-5}-10^{-4} s [50]. According to Pirro et al. [51], the interaction between self-trapped excitons (STEs) occurs in case of their high concentration in volume. The effect is described as a dipole-dipole interaction of the Auger type, when an exciton disappears with the transfer of its energy to another. The distance between the STEs should be as small as the value of the radius of the dipole-dipole interaction (Rd-d), which is to the order of a few nanometers, as was recently shown for some tungstates [52,53].

3.5. Photodegradation of methylene blue

According to literature [54], the photocatalytic activity of the molybdates is caused by the transfer of charge from the Orbital O 2p level of the Valence Band to the orbital Mo 4d empty level of the Conduction Band. The photocatalytic activity of $ZnMoO_4:Tb^{3+}$, Pr^{3+} on the methylene blue dye was evaluated, observing the effect of the dopants on the property. The increase in photocatalytic activity may be due to the entrapment of electrons photogenerated by dopants (Tb^{3+} and Pr^{3+}), reducing the recombination rate of electron-holes. According to the literature, this is a key factor for a good photocatalytic property [55].

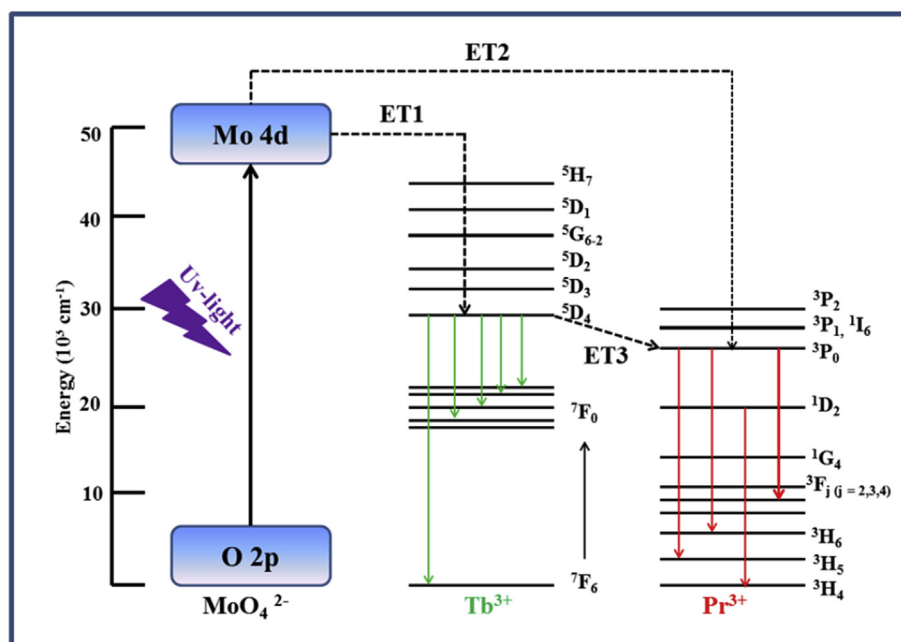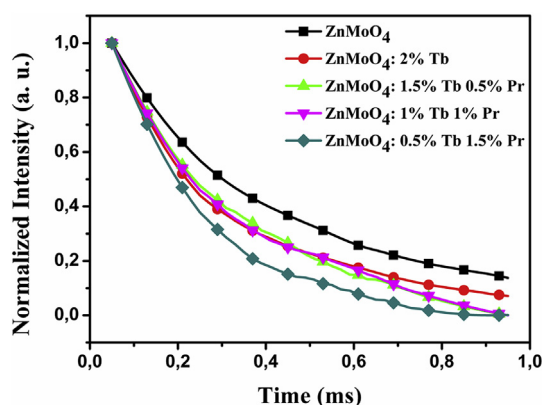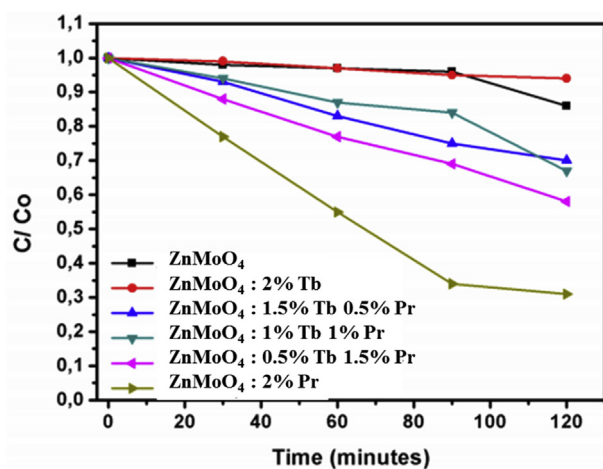A UV light source was used in the photocatalytic tests (E = 4.9 eV;

Fig. 8. Diagram of energy levels.

Fig. 9. The luminescence decay curves (excited at 350 nm and monitored at 545 nm) of ZnMoO$_4$:Tb^{3+}, Pr^{3+} phosphors with different Tb^{3+} and Pr^{3+} co-doping concentrations.

Fig. 10. Variation in the concentration of the methylene blue dye against the synthesized ZnMoO$_4$:Tb^{3+}, Pr^{3+} powders submitted to UV radiation. (For interpretation of the references to color in this figure legend, the reader is referred to the Web version of this article.)

$\lambda = 254$ nm) and the band gap energy of the ZnMoO$_4$:Tb^{3+}, Pr^{3+} particles is in the UV region, as shown in the reflectance results (E$_{gap}$ ~ 4.15 eV, $\lambda = 298$ nm) in Fig. 10. When ZnMoO$_4$ absorbs photons equal to or greater than its band gap energy, electrons are excited from the VB band to Conduction Band (CB), concomitantly leaving a "hole" in the VB of ZnMoO$_4$. These pairs of electron-holes normally recombine rapidly, so that the photocatalytic activity of the material decreases. This behavior is verified for the pure ZnMoO$_4$, presenting only 5% efficiency degradation. By modifying the electronic structure of ZnMoO$_4$ by doping with Tb^{3+} and Pr^{3+}, the electron excited in the Conduction Band can be captured by the dopants, which act as an electron trap and effectively separate the formation of electron pairs (e$^-$) - holes (h$^+$). The e$^-$ and h$^+$ photogenerates react with H$_2$O, O$_2$ and the organic substrate adsorbed on the photocatalytic surface to generate reactive species such as OH, O_2^-. The oxidative action of OH and O_2^- is able to decompose organic compounds into degradation products [56]. These radicals are involved in the processes of organic compound mineralization. From the results it can be seen that Pr^{3+} acts more effectively on the degradation of Methylene Blue, obtaining a better performance of the sample with 2% Pr which represented 70% degradation of the dye during 120 min of UV light irradiation. It can also be observed that the photocatalytic performance decreases as Tb^{3+} is added in the ZnMoO$_4$ structure. As for the sample with 2% Tb^{3+}, it did not show any performance regarding the degradation of methylene blue. It is reasonable to consider that the addition of Tb^{3+} promotes an increase in the recombination rate of e$^-$/h$^+$, inhibiting the photocatalytic activity. In addition to these results, photoluminescence is always used to clarify the photocatalytic performance of a semiconductor [57,58]. A strong PL intensity means that the photoinduced pairs e$^-$/h$^+$ are prone to recombine, thus reducing photocatalytic activity. As shown in the photoluminescence results, the ZnMoO$_4$:2% Tb^{3+} sample showed the highest PL intensity, as opposed to the results demonstrated in the photodegradation.

As shown in the study of ZnMoO$_4$:Tb^{3+}, Pr^{3+} morphologies, a change in the particle forms is observed from the type of dopant that is introduced into the structure of the zinc molybdate. It is known that other aspects regarding morphology, particle size and surface area are related to the photocatalytic performance of a material. Based on what was exposed in this study, it is reasonable to consider that the morphology type of ZnMoO$_4$:2% Pr^{3+} may have favored performance in

degradation tests.

4. Conclusion

The $ZnMoO_4$:Tb^{3+}, Pr^{3+} phosphor series was successfully produced by the sonochemical method. The XRD results showed the formation of the $ZnMoO_4$ particles which crystallized in the triclinic form without the presence of secondary phases. There is a more effective change in the morphology of the $ZnMoO_4$:2% Pr^{3+} particles in the form of nanorods due to a preferential particle growth. The emission spectra presented a strong contribution to the matrix under a 350 nm excitation with a broadband profile characteristic of the multiphonic process together with the specific transitions of Tb^{3+} and Pr^{3+}. The chromaticity coordinates were calculated based on the distributions of the PL spectra and the emissions were concentrated in the green and white regions. Possible processes of energy transfer between the matrix and the Tb^{3+} and Pr^{3+} ions were observed. Time resolved photoluminescence showed that the increase of Pr^{3+} favored the electronic interactions between Tb^{3+} and Pr^{3+} and resulted in a decrease of τ_{av}. The $ZnMoO_4$:2% Tb^{3+} sample had higher photoluminescent intensity, possibly due to its higher recombination rate ($\bar{e} + h$). The photocatalytic results showed that the addition of Pr^{3+} benefited the degradation of the methylene blue dye. The best result was for $ZnMoO_4$:2% Pr^{3+} sample with 70% efficiency for 2 h under UV radiation. This result can be attributed to the morphological characteristics presented by the $ZnMoO_4$:2% Pr^{3+} sample, as well as by the low recombination rate of the electron/hole pair.

Declaration of competing interest

The authors declare that they have no known competing financial interests or personal relationships that could have appeared to influence the work reported in this paper.

Acknowledgements

Appendix A. Supplementary data

Supplementary data to this article can be found online at https://doi.org/10.1016/j.optmat.2019.109332.

References

[1] M. Laguna, A.L. Becerro, M. Ocana, Morphology control of uniform CaMoO4 microarchitectures and development of white light emitting phosphors by Ln doping (Ln = Dy3+, Eu3+), CrystEngComm 19 (2017) 1590–1600.

[2] G.D. Wang, X.H. Gong, Y.J. Chen, J.H. Huang, Y.F. Li, Z.D. Luo, Y.D. Huang, Novel red phosphors KBaEu(XO4)3 (X = Mo,W) show high color purity and high thermostability from a disordered chained structure, Dalton Trans. 46 (2017) 6776–6784.

[3] S. Cotte, B. Pecquenard, F. le Cras, R. Grissa, L. Bourgeois, M.T. Sougrati, H. Martinez, Iron molybdate thin films prepared by sputtering and their electrochemical behavior in Li batteries, J. Alloy. Comp. 735 (2018) 1454–1462.

[4] X. Mua, Y. Zhanga, H. Wanga, B. Huanga, P. Suna, T. Chena, J. Zhoua, E. Xiea, Z. Zhang, A high energy density asymmetric supercapacitor from ultrathin manganese molybdate nanosheets, Electrochim. Acta 211 (2016) 217–224.

[5] Y. Zhu, Photocatalytic and luminescent properties of SrMoO4 phosphors prepared via hydrothermal method with different stirring speeds, J. Mater. Sci. Technol. 33 (2017) 23–29.

[6] H. Cao, N. Wu, Y. Liu, S. Wang, W. Du, J. Liu, Facile synthesis of rod-like manganese molybdate crystallines with two-dimensional nanoflakes for supercapacitor application, Electrochim. Acta 225 (2017) 605–613.

[7] F. Baur, F. Glocker, T. Jüstel, Photoluminescence and energy transfer rates and efficiencies in Eu3+ activated Tb3Mo3O12, J. Mater. Chem. C. 3 (2015) 2054–2064.

[8] R. Krishnan, J. Thirumalai, V. Mahalingam, S. Mantha, M. Lavany, Synthesis, luminescence and photometric characteristics of Ca0.5La(MoO4)2: Ln3+ (Ln = Eu, Tb, Dy) phosphors, Mater. Chem. Phys. 162 (2015) 41–49.

[9] N.S. Kozlova, A.P. Kozlova, E.V. Zabelina, Zh A. Goreeva, I.S. Didenko,

[10] V.M. Kasimov, A.G. Chernykh, Optical properties and microdefects in CaMoO4 single crystals, Crystallogr. Rep. 63 (2018) 216–221.

[10] L.X. Lovisa, J. Andrés, L. Gracia, M.S. Li, E. Longo, R.L. Tranquilin, C.A. Paskocimas, M.R.D. Bomio, F.V. Motta, Structure, morphology and photoluminescence emissions of ZnMoO4:RE3+ = Tb3+ - Tm3+ - X Eu3+ (x= 1, 1.5, 2, 2.5 and 3 mol%) particles obtained by the sonochemical method, J. Alloy. Comp. 750 (2018) 55–70.

[11] A.A.G. Santiago, C.R.R. Almeida, R.L. Tranquilin, R.M. Nascimento, C.A. Paskocimas, E. Longo, F.V. Motta, M.R.D. Bomio, Photoluminescent properties of the Ba1-xZnxMoO4 heterostructure obtained by ultrasonic spray pyrolysis, Ceram. Int. 44 (2018) 3775–3786.

[12] M. Ramezani, S.M. Sobhani-Nasab, A. Estarki, Synthesis, characterization, and morphological control of ZnMoO4 nanostructures through precipitation method and its photocatalyst application, J. Mater. Sci. Mater. Electron. 26 (2015) 7588–7594.

[13] N. Jaina, B.P. Singha, R.K. Singha, J. Singh, Enhanced photoluminescence behaviour of Eu3+ activated ZnMoO4 nanophosphors via Tb3+ co-doping for light emitting diode, J. Lumin. 188 (2013) 504–513.

[14] L.S. Cavalcantea, J.C. Sczancoskia, M.S. Li, E. Longo, J.A. Varela, β-ZnMoO4 microcrystals synthesized by the surfactant-assisted hydrothermal method: growth process and photoluminescence properties, Colloid. Surf. Physicochem. Eng. Asp. 396 (2012) 346–351.

[15] C. Arnaboldi, C. Brofferio, O. Cremonesi, L. Gironi, M. Pavan, G. Pessina, S. Pirro, E. Previtali, A novel technique of particle identification with bolometric detectors, Astropart. Phys. 34 (2011) 797–804.

[16] J. Fei, Q. Sun, J. Li, Y. Cui, J. Huang, W. Hui, H. Hu, Synthesis and electrochemical performance of α-ZnMoO4 nanoparticles as anode material for lithium ion batteries, Mater. Lett. 198 (2017) 4–7.

[17] V.B. Mikhailik, H. Kraus, D. Wahl, H. Ehrenberg, M.S. Mykhayl, Optical and luminescence studies of ZnMoO4 using vacuum ultraviolet synchrotron radiation, Nucl. Instrum. Methods Phys. Res. A 562 (2006) 513.

[18] G.M. Gurgel, L.X. Lovisa, O.L.A. Conceição, M.S. Li, E. Longo, C.A. Paskocimas, F.V. Motta, M.R.D. Bomio, Evaluation of morphology and photoluminescent properties of PbMoO4 crystals by ultrasonic amplitude, J. Mater. Sci. 52 (2016) 1–13.

[19] G.M. Gurgel, L.X. Lovisa, L.M. Pereira, F.V. Motta, M.S. Li, E. Longo, C.A. Paskocimas, M.R.D. Bomio, Photoluminescence properties of (Eu, Tb, Tm) co-doped PbMoO4 obtained by sonochemical synthesis, J. Alloy. Comp. 700 (2017) 130–137.

[20] X. Ju, X. Li, W. Li, W. Yang, C. Tao, Luminescence properties of ZnMoO4:Tb3+ green phosphor prepared via co-precipitation, Mater. Lett. 65 (2011) 2642.

[21] V.M. Longo, L.S. Cavalcante, E.C. Paris, J.C. Sczancoski, P.S. Pizani, M. Siu Li, J. Andres, E. Longo, J.A. Varela, Hierarchical assembly of CaMoO4 nano-octahedrons and their photoluminescence properties, J. Phys. Chem. C 115 (2011) 5207–5219.

[22] L. Yang, Y. Wang, Y. Wang, X. Wang, G. Han, Morphology-controlled synthesis of PbMoO4 crystals by a simple sonochemical method, J. Ceram. Soc. Jpn. 120 (2012) 609–612.

[23] J.M. Lifshitz, S.S. Slyozov, The kinetics of precipitation from supersaturated solid solutions, J. Phys. Chem. Solids 19 (1961) 35.

[24] E.J.H. Eduardo Lee, C. Ribeiro, E. Longo, E.R. Leite, Oriented attachment: an effective mechanism in the formation of anisotropic nanocrystals, J. Phys. Chem. B 109 (2005) 20842–20846.

[25] N.M. Ali, N.H. Rafat, Modeling and simulation of nanorods photovoltaic solar cells: a review, Renew. Sustain. Energy Rev. 68 (2017) 212–220.

[26] M. Kumar, V.S. Bhati, S. Ranwa, J. Singh, M. kumar, Pd/ZnO nanorods based sensor for highly selective detection of extremely low concentration hydrogen, Sci. Rep. 7 (2017) 1–9.

[27] M. Qiu, Z. Chen, Z. Yang, W. Li, Y. Tian, W. Zhang, Y. Xua, H. Cheng, ZnMn2O4 nanorods: an effective Fenton-like heterogeneous catalyst with t2g3eg1 electronic configuration, Catal. Sci. Technol. 8 (2018) 2557.

[28] M. Pal, U. Pal, M.J. Gracia, Y. Jiménez, F. Perez-Rodriguez, Effects of crystallization and dopant concentration on the emission behavior of TiO2: Eu nanophosphors, Nanoscale Res. Lett. 7 (2012) 1.

[29] I.M. Pinatti, P.F.S. Pereira, M. De Assis, E. Longo, I.L.V. Rosa, Rare earth doped silver tungstate for photoluminescent applications, J. Alloy. Comp. 771 (2019) 433–447.

[30] P. Kubelka, F. Munk-Aussig, Ein beitrag zur optick der farbanstriche, Z. Tech. Phys. 12 (1931) 593–601.

[31] R. Lacomba-Perales, J. Ruiz-Fuertes, D. Errandonea, A. Martinez-Garcia, Optical absorption of divalent metal tugstates: correlation between the band-gap energy and the cátion ionic radius, Eur. Physics Letters 83 (2008) 37002.

[32] I.L. Validzic, T.D. Savic, R.M. Krsmano, D.J. Jovanonic, M.M. Novakovic, M.C. Popovic, Synthesis, strong room temperature PL and photocatalytic activity of ZnO/ZnWO4 rod-like nanoparticles, Mater. Sci. Eng., B 177 (2012) 645.

[33] J. Ruiz-Fuertes, S. Lopez-Moreno, J. Lopez-Solano, D. Errandonea, A. Sefura, R. Lacomba-Perales, A. Munoz, S. Radescu, P. Rodriguez-Hernandez, L.L. Nagornaya, C.Y. Tu, Pressure effects on the electronics and optical properties of AWO4 wolframites (A = Cd, Mg, Mn and Zn): the distinctive behavior of multiferroic, Phys. Rev. B. 86 (2012) 125202.

[34] E. Longo, D.P. Volanti, V.r.M. Longo, L. Gracia, I.a.C. Nogueira, M.A. Almeida, A.N. Pinheiro, M.M. Ferrer, L.c.S. Cavalcante, J. Andr_es, Toward an understanding of the growth of Ag filaments on α-Ag2WO4 and their photoluminescent properties: a combined experimental and theoretical study, J. Phys. Chem. C 118 (2014) 1229–1239.

[35] D.A. Spassky, A.N. Vasil'ev, I.A. Kamenskikh, V.V. Mikhailin, A.E. Savon, Y.A. Hizhnyi, S.G. Nedilko, P.A. Lykov, Electronic structure and luminescence mechanisms in ZnMoO4 crystals, J. Phys. Condens. Matter Inst. Phys. J. 23 (2011) 365501.

[36] W. Zhang, J. Yin, F. Min, L. Jia, D. Zhang, Q. Zhang, J. Xie, Preparation and photoluminescence properties of MMoO4 (M = Cu, Ni, Zn) nano-particles synthesized via electrolysis, J. Mol. Struct. 1127 (2017) 777–783.

[37] B.G. Zhai, Q.I. Ma, L. Yang, Y.M. Huang, Effects of sintering temperature on the morphology and photoluminescence of Eu^{3+} doped zinc molybdenum oxide hydrate, J. Nanomater. 2018 (2018) 7418508.

[38] V.M. Longo, L.S. Cavalcante, R. Erlo, V.R. Mastelaro, A.T. Figueiredo, J.R. Sambrano, S. Lazaro, A.Z. Freitas, L. Gomes, N.D. Vieira Jr., J.A. Varela, E. Longo, Strong violet–blue light photoluminescence emission at room temperature in $SrZrO_3$: joint experimental and theoretical study, Acta Mater. 56 (2008) 2191.

[39] Z. Xianju, Y. Xiaodong, X. Tengjiao, Z. Kaining, C. Tianyu, Y. Hao, W. Zhongqing, Luminescence properties and energy transfer of host sensitized $CaMoO_4$:Tb^{3+} green phosphors, J. Rare Earths 31 (2013) 655–659.

[40] J.C. Sczancoski, L.C. Cavalcante, N.L. Marana, R.O. Silva, R.L. Tranquilin, M.R. Joya, J.A. Varela, J.R. Sambrano, M. Siu Li, E. Longo, J. Andrés, Electronic structure and optical properties of $BaMoO_4$ powders, Curr. Appl. Phys. 10 (2010) 614–624.

[41] J. Liao, S. Lin, L. Zhang, N. Pan, X. Cao, Photocatalytic degradation of methyl orange using a TiO_2/Ti mesh electrode with 3D nanotube Array, ACS Appl. Mater. Interfaces 4 (2012) 171–177.

[42] L.S. Cavalcante, J.C. Sczancoski, M. Siu Li, E. Longo, J.A. Varela, $ZnMoO_4$ microcrystals synthesized by the surfactant-assisted hydrothermal method: growth process and photoluminescence properties, Colloids Surf., A 396 (2012) 346–351.

[43] A.B. Campos, A.Z. Simões, E. Longo, J.A. Varela, V.M. Longo, A.T. Figueiredo, F.S. Vicente, Mechanisms behind blue, green, and red photoluminescence emissions in $CaWO_4$ and $CaMoO_4$ powders, Appl. Phys. Lett. 91 (2007) 051923.

[44] A.P.A. Marques, F.V. Motta, E.R. Leite, P.S. Pizani, J.A. Varela, E. Longo, D.M.A. Melo, Evolution of photoluminescence as a function of the structural order or disorder in $CaMoO_4$ nanopowders, J. Appl. Phys. 104 (2008) 043505.

[45] J. Andrés, E. Longo, J.A. Varela, Hierarchical assembly of $CaMoO_4$ nanooctahedrons and their photoluminescence properties, J. Phys. Chem. C 115 (2011) 5207e5219.

[46] Y. Zhang, N.A.W. Holzwarth, R.T. Williams, Electronic band structures of the scheelite materials $CaMoO_4$, $CaWO_4$, $PbMoO_4$, and $PbWO_4$, Phys. Rev. B 57 (1998) 12738e12750.

[47] Y. Zhai, Q. Sun, S. Yang, Y. Liu, J. Wang, S. Ren, S. Ding, Morphology-controlled synthesis and luminescence properties of green-emitting $NaGd(WO_4)_2$:Tb^{3+} phosphors excited by n-UV excitation, J. Alloy. Comp. 781 (2019) 415–424.

[48] D. Zeng, Y. Chen, Y. Cai, C. Peng, S. Peng, Synthesis and luminescence of Pr^{3+} doped Lu_2MoO_6 phosphors, J. Lumin. 206 (2019) 376–379.

[49] L.X. Lovisa, A.A.G. Santiago, M.F. Farias, B.S. Barros, E. Longo, M. Siu Li, P.A. Paskocimas, M.R.D. Bomio, F.V. Motta, White light emission from single-phase Y_2MoO_6: xPr^{3+} (x = 1, 2, 3 and 4 mol%) phosphor, J. Alloy. Comp. 769 (2018) 420–429.

[50] F.A. Danevich, Development of crystal scintillators from enriched isotopes for DoubleβDecay experiments, IEEE Trans. Nucl. Sci. 59 (2012) 2207–2213.

[51] S. Pirro, J.W. Beeman, S. Capelli, M. Pavan, E. Previtali, P. Gorla, Scintillating double-beta-decay bolometers, Phys. At. Nucl. 69 (2006) 2109–2116.

[52] S. Markov, V. Nagirnyi, A. Vasil'ev, V. Makhov, R. Laasner, S. Vielhauer, M. Kirm, R. Grigonis, V. Sirutkaitis, Modelling of decay kinetics of self-trapped exciton luminescence in $CdWO_4$ under femtosecond laser excitation in absorption saturation conditions, Cent. Eur. J. Phys. 10 (2012) 1002–1008.

[53] G. Bizarri, W.W. Moses, J. Singh, A.N. Vasil'ev, R.T. Williams, The role of different linear and non-linear channels of relaxation in scintillator non-proportionalit, J. Lumin. 129 (2009) 1790–1793.

[54] L.S. Cavalcante, N.C. Batista, E. Longo, J.A. Varela, M.O. Orlandi, Growth mechanism and photocatalytic properties of $SrWO_4$ microcrystals synthesized by injection of ions into a hot aqueous solution, Adv. Powder Technol. 24 (2013) 344–353.

[55] L.S. Cavalcante, M.A.P. Almeida, A.C. Rabelo, I.C. Nogueira, N.C. Batista, Structural refinement, growth process, photoluminescence and photocatalytic properties of $(Ba_{1-x}Pr_{2x/3})WO_4$ crystals synthesized by the coprecipitation method, RSC Adv. 2 (2012) 6438–6454.

[56] Y.R. Jiang, W.W. Lee, K.T. Chen, M.C. Wang, K.H. Chang, C.C. Chen, Hydrothermal synthesis of β-$ZnMoO_4$ crystals and their photocatalytic degradation of Victoria Blue R and phenol, J Taiwan Inst. Chem. E. 45 (2014) 207–218.

[57] T. Montini, A. Hameed, L. Felisari, G. Adami, P. Fornasiero, Synthesis, characterization and photocatalytic performance of transition metal tungstates, Chem. Phys. Lett. 498 (2010) 113.

[58] K. Rajeshwar, W. Chanmanee, C.R. Chenthamarakshan, M.V.B. Zanoni, P. Kajitvichyanukul, Heterogeneous photocatalytic treatment of organic dyes in air and aqueous media, J. Photochem. Photobiol., A C 9 (2008) 171–192.